Published in final edited form as:
Neuron. 2014 February 5; 81(3): 616–628. doi:10.1016/j.neuron.2013.11.020.

Temporal responses of *C. elegans* chemosensory neurons are preserved in behavioral dynamics

Saul Kato[1], **Yifan Xu**[2], **Christine E. Cho**[2], **L. F. Abbott**[1], and **Cornelia I. Bargmann**[2]

[1]Department of Neuroscience and Department of Physiology and Cellular Biophysics, Columbia University College of Physicians and Surgeons, New York, New York, USA.

[2]Howard Hughes Medical Institute, The Rockefeller University, New York, New York, USA.

Summary

Animals track fluctuating stimuli over multiple timescales during natural olfactory behaviors. Here, we define mechanisms underlying these computations in *Caenorhabditis elegans*. By characterizing neuronal calcium responses to rapidly fluctuating odor sequences, we show that sensory neurons reliably track stimulus fluctuations relevant to behavior. AWC olfactory neurons respond to multiple odors with sub-second precision required for chemotaxis, whereas ASH nociceptive neurons integrate noxious cues over several seconds to reach a threshold for avoidance behavior. Each neuron's response to fluctuating stimuli is largely linear, and can be described by a biphasic temporal filter and dynamical model. A calcium channel mutation alters temporal filtering and avoidance behaviors initiated by ASH on similar timescales. A sensory G-alpha protein mutation affects temporal filtering in AWC, and alters steering behavior in a way that supports an active sensing model for chemotaxis. Thus temporal features of sensory neurons can be propagated across circuits to specify behavioral dynamics.

Introduction

Olfactory, gustatory, and pheromone cues provide essential information about an animal's environment. Because these cues are chemically diverse, most studies of the chemical senses ask how animals detect and distinguish the chemical identity of a stimulus. However, the temporal properties of stimuli are also important, conveying information about the distribution of food, mates, competitors, and predators (Koehl and Reidenbach, 2011; Riffell et al., 2008). Accordingly, the olfactory system should detect temporal features of chemical stimuli, just as neurons in the visual and auditory systems are tuned to relevant temporal features (DeAngelis et al., 1995; Nagel and Doupe, 2008). Temporal response characteristics of olfactory neurons and their targets have been studied in a variety of animals (Bhandawat et al., 2005; Brown et al., 2005; Geffen et al., 2009; Getahun et al., 2012; Kim et al., 2011;

Correspondence: lfa2103@columbia.edu, cori@rockefeller.edu.

Martelli et al., 2013; Nagel and Wilson, 2011; Shusterman et al., 2011; Vickers et al., 2001), but the detailed relationships between neuronal dynamics and behavioral timescales have not been defined.

In the nematode worm *Caenorhabditis elegans*, chemosensation and chemosensory behaviors can be functionally mapped to individual genes and neurons (Bargmann, 2006). Each sensory neuron detects environmental chemicals through a cell type-specific repertoire of G protein-coupled receptors, and directs characteristic behaviors such as chemotaxis or avoidance. These behaviors require the integration of chemical cues over a range of timescales. For example, during gradient climbing animals follow odor concentration changes within a few seconds to regulate their head orientation, but they also integrate concentration changes over about a minute to regulate turning frequency (Pierce-Shimomura et al., 1999; Iino and Yoshida, 2009; Izquierdo and Lockery, 2010; Albrecht and Bargmann, 2011); in avoidance behaviors, animals withdraw from a strong noxious stimulus within a second, but integrate weak noxious stimuli over about ten seconds (Chao et al., 2004).

Sensory neurons are tuned to chemical identity by the receptor genes they express, but to establish a link to behavioral timescales, we must examine their temporal response properties. Direct examination of chemosensory signaling in *C. elegans* using genetically-encoded calcium indicators has shown that sensory neurons respond to chemical stimuli with a slow calcium transient that rises for several seconds and decays partially or completely over ∼60s of stimulus presentation (Hilliard et al., 2005; Chalasani et al., 2007; Suzuki et al., 2008; Zimmer et al., 2009; Busch et al., 2012). The stronger initial calcium response and weaker tonic response of sensory neurons correlates with their ability to drive both immediate and prolonged behavioral responses (Chalasani et al., 2007; Zimmer et al., 2009; Busch et al., 2012), but beyond that, the nature of temporal encoding is a mystery.

Here, we characterize temporal coding in two classes of *C. elegans* chemosensory neurons: AWC neurons that sense attractive odorants and ASH neurons that sense noxious chemical and mechanical stimuli. We show that these neurons respond reliably and robustly at speeds that are well matched to their particular behavioral functions. Models of their temporal properties provide insight into the defects caused by sensory signal transduction mutations and demonstrate a close relationship between sensory neuron dynamics and sensory-driven behaviors.

Results

Reliable responses to rapid stimulus fluctuations

We developed and validated a system for simultaneous calcium imaging and delivery of rapidly fluctuating odor stimuli (5 Hz) in an all-liquid environment in a microfluidic chip (Figure S1). We monitored the activity of *C. elegans* sensory neurons to these fluctuating stimuli using the genetically encoded calcium indicator GCaMP3 (Tian et al., 2009), which has high sensitivity (660 nM apparent affinity), a ∼10-fold dynamic range, and rapid dynamics (344 ms $t_{1/2}$ decay time)(Sun et al., 2013). Calcium imaging is well-suited to *C. elegans* neurons, which typically have graded responses, lack sodium-based action

potentials, and use voltage-gated calcium channels to amplify neuronal inputs and regulate neurotransmitter release (Goodman et al., 1998; Liu et al., 2009).

The AWC olfactory neurons, which mediate chemotaxis to attractive odors, are inhibited by odors and activated by odor removal (Chalasani et al., 2007). Removing the attractive odor isoamyl alcohol after a five-minute exposure results in a calcium increase in AWC that peaks within 5 s and decays over 30-60 s (Figure 1A). When the five-minute pulse was instead followed with alternating 1 s pulses of odor and buffer, AWC responded with regular, sustained calcium oscillations at 0.5 Hz (Figure 1C). The oscillating response followed the stimulus with a reliable phase lag near 90°, continued after the OFF response reached a steady state (Figure 1C, inset), and stopped immediately when stimulus oscillations ceased.

ASH nociceptive neurons respond to noxious chemicals such as high-osmolarity glycerol with an increase in calcium that peaks within 10 s and decays over 60 s (Hilliard, et al. 2005) (Figure 1B). Replacing the glycerol step stimulus with a flickering 1 s glycerol stimulus resulted in regular oscillations of the calcium signal at 0.5 Hz, delayed by a >180° phase shift relative to the stimulus, that persisted after the decay of the initial ON response (Figure 1D). Thus, AWC and ASH neurons can respond to sub-second stimulus fluctuations.

To characterize the temporal features of the AWC and ASH responses more precisely, we used a system identification approach. Transitions between full and zero odor concentration were controlled by a pseudo-random m-sequence to approximate a spectrally unbiased stimulus pattern (Figure 1E,F, Experimental Procedures). Both AWC and ASH responded to the m-sequence stimuli with calcium fluctuations that persisted after the initial response to stimulus onset or offset reached steady state (Figure 1E,F). These AWC and ASH calcium responses were strikingly stereotyped across different animals and across trials for a given animal (Figure 1G,H, Experimental Procedures, and data not shown); AWC responses had a finer temporal resolution than ASH.

Linear temporal filters describing AWC and ASH sensory neurons

The steady-state responses to m-sequence stimuli (Figure 1E,F, **brackets**) provided a basis for modeling the input-output transformations of AWC and ASH neurons as linear-nonlinear (L-N) cascades (Experimental Procedures)(Dayan and Abbott, 2001; Westwick and Kearney, 2003; Sakai et al., 1988). In this approach, the input-output transformation for each neuron is decomposed into two sequential operations: convolution with a linear temporal filter that describes how the recent history of the stimulus contributes to the current value of an intermediate variable *x* at time *t*, followed by the application of a static nonlinearity that converts *x(t)* into an estimate of the measured fluorescence change (Figure S2A).

Consistent linear temporal filters for AWC and ASH were extracted from single trials (gray traces in Figure 2A) and from trial-averaged data (black traces in Figure 2A). The temporal filters for ASH and AWC are shown with opposite signs, reflecting the fact that ASH activity rises and AWC activity falls in response to stimulus increases. The trial-averaged filter for AWC has an initial component that peaks at 0.9 s and decays with a $t_{1/2}$ of 1.5 s (n=11, range t_{peak}= 0.6 - 1.15 s, $t_{1/2}$ = 0.8 - 2.1 s); the trial-averaged filter for ASH peaks at

3.4 s and decays with a $t_{1/2}$ of 4.3 s (n=13, t_{peak}= 2.9 - 3.6 s, $t_{1/2}$ = 2.8 - 6.1 s) (Figure 2A). Close inspection of AWC and ASH filters suggested that each is biphasic, and switches its sign after lags greater than 10-12 s for AWC and greater than ∼15 s for ASH. Modeling work and responses to step stimuli described below support the existence of these features.

The temporal filters for both AWC and ASH were reproducible when derived using a second m-sequence with a different detailed structure (Figure 2B). In addition, exposing AWC to an m-sequence without the initial 5-minute odor pre-exposure yielded a temporal filter indistinguishable from that obtained with the standard odor protocol (Figure 2C). In control experiments, similar temporal filters were observed in animals whose GCaMP3 expression levels varied by ∼5 fold (not shown), and in an AWC strain expressing a different calcium indicator, GCaMP5A (Figure 2C). These results suggest that the temporal filters are robust to the detailed pattern of stimulation, as well as the expression level and type of reporter protein. AWC responded reliably to the m-sequence of isoamyl alcohol over a 100-fold range of concentrations, in each case yielding a similar temporal filter (Figure 2C). Similarly, ASH filters were consistent over an 8-fold concentration range of osmotic glycerol stimuli (Figure S3B). These results suggest that temporal filtering in AWC and ASH is independent of stimulus intensity across a broad range of concentrations.

Somatic calcium responses are not always correlated with electrical activity, but calcium entry through voltage-gated channels in presynaptic axons is tightly associated with synaptic transmission and neuronal output. A comparison of axonal and somatic calcium signals tracked with GCaMP3 showed that axonal calcium for each neuron had a similar temporal filter to the cell body, but with slightly faster rise to peak (AWC: 0.85→0.6 s, ASH: 3.5→3.1 s), and a significantly shorter half-width (AWC: 2.3→1.4 s, ASH: 6.3→5.0 s) (Figure 2D,E). The overall match between these filters suggests that calcium signals in AWC and ASH are relatively consistent across the cell under these conditions, although slightly slower in the soma.

An ODE model defines separate contributions of neuronal signaling and GCaMP dynamics

We modeled the phenomenological filters for AWC and ASH neurons as a sum of three exponential functions generated by a system of three first-order linear ordinary differential equations, the “ODE model” (Figure 3A,B, Experimental Procedures). The model consists of an initial process (**A** in Figure 3B) that reproduces the response rise time, followed by two parallel paths of opposite sign with fast and slow dynamics (**F** and **S**). The relative timescales of the fast and slow components are primarily set by the relaxation time constants $1/k_f$ and $1/k_s$ of the parallel path variables, and their relative strengths are set by the forward interaction rate constants k_{af} and k_{as} (Figure 3B). After parameter optimization, the sensory filters given by this model closely matched the trial-averaged filters extracted from the data (Figure 3C, Table S1). The model filters are the sum of two components, one arising from the A-F pathway and the other from the A-S pathway (Figure 3D).

The temporal filters extracted directly from input-output records reflect the response properties of the neurons as well as the dynamics of the conversion of intracellular calcium levels into fluorescence signals by the GCaMP indicator (Figure 3A). To estimate the intrinsic neuronal filters, which are not directly observable, we modeled the effects of

GCaMP as an additional L-N cascade that captures the known calcium binding and unbinding properties of GCaMP3 (Tian et al., 2009; Sun et al., 2013)(Experimental Procedures), and then deconvolved the observed sensory filter with the linear GCaMP element. In doing this, it was important to use the analytically smooth filters described by the ODE model, because the required deconvolution amplifies high-frequency noise in sampled data, whereas the deconvolution of the ODE model filter can be done exactly (Experimental Procedures). The results of this deconvolution suggested that the intrinsic AWC filter peaks very rapidly: the first component peaks within 0.35 s of stimulus onset in the soma (Figure 3E), and at 0.15 s in the axon. Similar calculations suggested that the intrinsic ASH filter peaks at 2.9 s in the soma (Figure 3E) and 2.25 s in the axon.

The nonlinearities that convert the filtered signal into the observed fluorescence changes for both AWC and ASH had similar, monotonic, concave forms (Figure 3F, S2B-E, S3B). The mean exponent of a power-law function fit to this nonlinearity was 2.3 for AWC and 1.8 for ASH (Experimental Procedures, Figure S2B-E), near the Hill coefficient of 2.3 describing the cooperative dependence of GCaMP3 fluorescence intensity on calcium binding (Tian et al., 2009). This match suggests that a substantial component of the observed nonlinear response function is due to the calcium-to-fluorescence transformation of GCaMP3. In turn, this implies that the intrinsic calcium responses of AWC and ASH are close to linear over the tested range.

L-N models accurately predict neuronal responses

The empirically derived temporal filters (Figure 2A) and the filters described by the ODE model (Figure 3C) were validated by using them to predict neuronal responses to experimental stimuli. For each individual recording, we derived an L-N model from the neuronal response (grey traces in Figure 2A), and used this model to generate a simulated response to the measured input stimulus. We also used the trial-averaged L-N model for AWC or ASH (black traces in Figure 2A) to simulate each response. In all cases the simulation closely matched the true neuronal response, with similar performance for individual and trial-averaged models, indicating that trial-by-trial fitting was not required for good model results (Figure 4A,B). The trial-averaged L-N models performed equally well on an independent set of trials that were not used for filter estimation (Figure 4B). Finally, we observed similar accuracy when we cross-validated the L-N model derived from one m-sequence to test data using a second m-sequence (Figure 2B, 4B). These results compare favorably to L-N model fitting in other experimental systems (Geffen et al., 2009, Clark et al., 2011).

The ODE filter model is described by seven free parameters, four describing the normalized linear temporal response and three describing the (GCaMP) power law nonlinearity. Using the same approach described above, we derived a model for each individual trace and the trial-averaged trace, and used these models to simulate responses to inputs. The average variance accounted for by the ODE filters for each neuron was 69-96% (individualized model) or 61-96% (trial-averaged model) (Figure 4B). The ODE model generated from trial-averaged data performed equally well at explaining variance when cross-validated with independent experimental trials and m-sequences (Figure 4B). The success of these ODE

models indicates that the good performance of the empirically derived filters for the L-N models did not arise from overfitting.

The filters predict additional features of AWC and ASH responses

To test the generality of the LN-ODE models for stimuli other than the m-sequence, we used the LN-ODE model to simulate the calcium response to 1 s flickering stimuli in AWC and ASH neurons, using the measured trial-averaged input stimulus as input to the model (Figure 1C,D). The model accurately predicted the relative magnitude and the phase lag of both AWC and ASH responses to 1 s flickers, showing a larger magnitude oscillatory response in AWC than in ASH and a distinct phase lag in ASH (Figure 4C,D).

Remarkably, the simulated traces also provide a good description of the initial onset/offset responses in AWC and ASH (Figure 4C), even though the models were constructed solely from data taken during the later steady-state period of the response. The LN-ODE model captured large initial responses to stimulus offset or onset, the timing of the response peak, the initial decay of the response, and the sustained response fluctuations (Figure 4C). The ability of the models to account for the initial transient is due to the biphasic structure of their temporal filters, with components of different sign and width, and can be understood by picturing how a step stimulus is integrated by the filter (Figure S4). The step first encounters the initial rise and peak of each filter, resulting in the initial rise of the response. A purely monophasic filter would result in a monotonic response, but the response to a biphasic filter with fast and slow components of opposite sign decays as the contribution from the slow component becomes more prominent (Figure S4). This allows the model to predict a response decay after the peak, a feature that resembles adaptation (Figure 4C, Figure S4).

For both neurons, but especially for ASH, the model overestimates the steady-state fluorescence level and the flicker magnitude of the response at long times (> 60 s for AWC and > 40 s for ASH) (Figure 4C). This discrepancy suggests the existence of additional sensory adaptation mechanisms that are not accounted for by the LN-ODE model (Figure S4); multiple adaptation mechanisms are a common feature of sensory responses (e.g. Fairhall et al., 2001). In addition, the model underestimates the initial slope (<5s) of the responses for both AWC and ASH. These two discrepancies may be related, because sensory responses tend to be both larger and faster before adaptation.

Generalization of the sensory filters across odors

To determine whether AWC response properties generalize across odors, we examined two additional odors, benzaldehyde and butanone. Both are sensed by AWC, but genetic and behavioral evidence suggests that they are detected through different receptors than isoamyl alcohol (Bargmann, 2006; Wes and Bargmann, 2001). AWC responded strongly and reliably to m-sequences of either butanone or benzaldehyde, yielding average temporal filters similar to the average filter for isoamyl alcohol (Figure 4E,F). This similarity suggests that rapid linear sensory processing may be a general feature of AWC.

ASH neurons are polymodal nociceptors that detect aversive touch, osmolarity, acid, odors, and tastes, in each case mediating reversal behaviors. We found that ASH responses to high

osmolarity NaCl (500 mM) could be described with a temporal filter similar to the filter obtained with glycerol (Figure 4G). By contrast, ASH responses to copper (1-10 mM $CuCl_2$), quinine (10 mM), and dihydrocaffeic acid (DHCA, 100-300 μM) adapted quickly and did not support sustained responses to fluctuating stimuli (Figure S5A and data not shown). These results suggest that ASH response dynamics are less stereotyped than those of AWC.

A calcium channel mutant probes the mechanisms and behavioral impact of ASH response dynamics

ASH neurons detect chemical repellents using multiple G protein-coupled receptor proteins, heterotrimeric G proteins, and channels of the TRPV family, whose opening secondarily activates the voltage-gated calcium channel EGL-19 (Figure S3A). For the most part, sensory transduction genes required for glycerol avoidance behavior were also required for ASH calcium responses to 10s glycerol pulses and to fluctuating m-sequence stimuli – for example, the sensory G protein *odr-3* and the TRPV channels *osm-9 ocr-2* (Figure S5 and data not shown). These results suggest that a common sensory transduction cascade initiates ASH calcium responses to both sustained and flickering glycerol stimuli.

The L-type voltage-gated Ca^{2+} channel encoded by *egl-19* had a more subtle role in ASH signaling. The magnitude of ASH calcium responses to 1 M glycerol was only slightly decreased by an *egl-19(n582)* reduction-of-function mutation, but ASH dynamics were different from the wild type, with a delayed peak and less decay during either prolonged or sequential presentations of glycerol stimuli (Figure 5A, Figure S5). This effect was clarified by exposing *egl-19(n582)* ASH neurons to glycerol stimuli presented in the m-sequence and extracting the temporal filter (Figure 5B-D). ASH neurons in *egl-19(n582)* mutants appeared monophasic, lacking the inverted, slow component of the linear filter (component A-S in Figure 3B,D) and retaining only the fast A-F component (Figure S3D). The ODE model predicts that the absence of the slower A-S component should delay the peak calcium response and reduce response decay after long glycerol pulses, matching the observed ASH response (Figure 5A). Conversely, an *egl-19(ad695gf)* gain-of-function mutant appeared to enhance the slow inhibitory component of the ASH response, leading to an opposite effect on the temporal filter (Figure 5B-D, S3).

These results implicate calcium entry through the EGL-19 voltage-gated Ca^{2+} channel in the decay of the ASH sensory response after ∼15 seconds. To ask whether these properties were represented in avoidance behavior, we quantified avoidance behaviors in a microfluidic chip that allowed rapid addition and removal of glycerol with simultaneous tracking of behaviors in many animals (Albrecht and Bargmann, 2011). Wild-type animals responded to glycerol with turns and reversals that diminished in frequency within a 30 s stimulus pulse, suggesting behavioral adaptation, and with transient slowing of forward locomotion that recovered fully during the 30 s pulse (Figure 5E-G). In *egl-19(n582)* mutants, initial glycerol avoidance behaviors were normal, but adaptation of turns, reversals, and locomotion speed was significantly delayed, resulting in sustained avoidance (Figure 5E-G). Thus, *egl-19* has matching effects on calcium response dynamics in ASH and behavioral adaptation to aversive stimuli on similar timescales.

Rapid AWC-dependent signaling is associated with a specific chemotaxis strategy

The dynamic analysis described above implies that AWC can process odor fluctuations in less than a second, much more rapidly than was expected from previous calcium imaging experiments. One rationale for this property is suggested by considering the two strategies *C. elegans* uses for chemotaxis (Figure 6A). In the "pirouette" strategy, animals integrate odor history over 20-90 seconds to regulate a biased random walk, and suppress turns when approaching an odor (Pierce-Shimomura et al., 1999). In the alternative "weathervane" or klinotaxis strategy, animals make small directed course corrections to steer upward in a gradient (Iino and Yoshida, 2009; Albrecht and Bargmann, 2011). A theoretical model for directed steering has suggested that the animal could sample the environment through the head swings generated during its own sinusoidal motion, as long as odor sensation rises and falls within ∼0.5-1 s, the timescale of one head swing (Izquierdo and Lockery, 2010)(Figure 6G).

The importance of the rapid AWC filter in these chemotaxis strategies was addressed by identifying a mutant that affects the fast odor responses of the AWC neurons. Animals mutant for the G protein alpha subunit ODR-3 are defective in their ability to chemotax to isoamyl alcohol, but retain a partial ability to chemotax to butanone (Roayaie et al., 1998). AWC neurons in *odr-3* mutants responded reliably to fluctuating isoamyl alcohol and butanone stimuli (Figure 6B). However, the *odr-3* isoamyl alcohol filter was considerably slowed; after correcting for GCaMP dynamics, the time to peak averaged 1.5 sec (Figure 6B-D). The *odr-3* butanone filter was less strongly affected, peaking in <1 sec (Figure 6C,D). The rapid AWC response to isoamyl alcohol was rescued by expressing an *odr-3* cDNA in AWC neurons, confirming that the defect was caused by the *odr-3* mutation (Figure S6). These results suggest that an ODR-3-containing G protein is required for very rapid AWC calcium responses to the same odor for which *odr-3* affects chemotaxis.

The ∼1.5 sec response of *odr-3* AWC neurons to isoamyl alcohol is predicted to be above the range required for rapid steering, but within the longer range required for regulation of turning rates. We therefore assessed both rapid steering and regulated turning by wild-type and *odr-3* animals in a gradient of isoamyl alcohol. Wild-type and *odr-3* mutants had comparable performance in "pirouette" or turning behaviors (Figure 6E). Wild-type animals also showed accurate steering toward the isoamyl alcohol, as demonstrated by a curving rate that peaked when the animal's bearing was 90° from the odor source. By contrast, *odr-3* mutants were defective in steering when heading ≥ 90° from the odor source (Figure 6F). These results support the possibility that rapid AWC responses contribute to rapid steering behavior in chemotaxis.

In the presence of a spatial gradient, head swings should cause an oscillation in odor concentration at the tip of the nose that is proportional to head motion (Figure 6G). We modeled the concentration oscillations experienced as a result of head swings when an animal is oriented 90° from the odor source, and then used L-N models derived from wild-type and mutant animals to predict AWC responses to the oscillating stimulus (Figure 6G, lower panel). The predicted AWC oscillations for *odr-3* mutants were smaller in amplitude

than those for the wild type and more phase-shifted with respect to the odor gradient, in agreement with a chemotaxis defect.

Both amplitude and phase information could be exploited to guide locomotion in a gradient. A simple model of how the animal determines steering angles was used to explore how these signals might be used in chemotaxis. With respect to phase information, when the heading angle of the animal relative to the odor source is θ, the signal obtained from the difference between the AWC responses during dorsal and ventral swings is proportional to sin(θ). The sinusoidal shape of the wild-type curving rate trace (Figure 6F) suggests that this phasic "difference signal" is relevant for steering behavior. *odr-3* mutants regulate their curving rates based on bearing, but do so incorrectly. A possible explanation is that they detect oscillations in AWC responses during head swings but, because of the increased phase delay (Figure 6G), cannot determine which side corresponds to the higher concentration. The behavior we observe suggests that they instead use an amplitude-based strategy, steering in the direction that reduces the magnitude of the AWC oscillations. In other words, the mutants may use the gradient of the magnitude $\sin^2(\theta)$ to guide their behavior, which means that the relevant signal is $d\sin^2(\theta)/d\theta = \sin(2\theta)$. The curving rate of the mutant animals (Figure 6F) is well-approximated by a constant times sin(2θ), suggesting that, being unable to interpret the phase of the signal, they use changes in its amplitude to direct their steering.

Discussion

AWC and ASH neurons encode sensory information through rapid, precise signal processing over less than a second (AWC) or a few seconds (ASH), with a near-linear transformation of sensory information into calcium signals. They also respond to stimulus offset or onset with a large calcium peak that decays to steady-state over tens of seconds. The rapid responses and a significant component of the initial peak and decay can be described by a single biphasic filter expressed in terms of three decaying exponentials and a simple kinetic scheme. Through the use of mutants, we were able to relate the filters downward to the molecular signaling pathways that generate them and upward to the behaviors that they support.

Biphasic filters of this general form, with the first and second phases having different timescales, are found in sensory systems ranging from bacterial chemotaxis to human psychophysics. An analysis of responses to step inputs offers an intuitive way to understand a filter's effect (Figure S4). A purely monophasic filter reports the strength of a stimulus, a biphasic filter with phases of equal area can generate perfect adaptation, and a partially biphasic filter can reach a steady state that represents average stimulus intensity while maintaining sensitivity to stimulus fluctuations. In the context of bacterial chemotaxis, the separated-timescale biphasic filter has been proposed as an optimal fitness balance between the goals of reaching locations of maximum attractant and the speed of gradient climbing (Segall et al., 1986; Clark and Grant, 2005). As a temporal receptive field in mammalian vision, this shape has been proposed as a balance between the decorrelation of stimulus redundancy and filtering of noise for the purpose of efficient neural coding (Atick and Redlich 1990).

After correction for the nonlinearity of the GCaMP3 indicator, the responses of AWC and ASH neurons were approximately linear. This linearity may result from the fact that these non-spiking neurons are not subject to nonlinear spike thresholds, and therefore can take advantage of the greater coding capacity inherent in analog rather than digital signaling. More generally, linear or near-linear encoding is common in early steps of sensory processing, as is analog signaling. Sensory responses are largely linear in invertebrate and vertebrate photoreceptors (Marmarelis and McCann, 1977; Schnapf et al., 1990), in rat trigeminal neurons (Jones et al., 2004) and in primate vestibular neurons (Massot et al., 2012), with more complex features emerging in higher-order neurons.

Temporal filtering of olfactory information

The question of how olfactory systems represent or use temporal information from odor fluctuations to guide behavior has long been of interest, but has been difficult to address directly in other animals because of the many steps between odor sensation and behavior. For example, system identification approaches have revealed highly heterogenous temporal properties of insect olfactory neurons (Getahun et al., 2012; Kim et al., 2011; Martelli et al., 2013; Nagel and Wilson, 2011). Not only are individual neurons different from one another, but a single neuron expressing a single receptor protein can respond to two different odors with distinct temporal dynamics. This heterogeneity helps encode odor identity, as flies can behaviorally discriminate two odors that activate the same receptor with different dynamics (DasGupta and Waddell 2008). Whether these heterogeneous properties also relay odor-specific information about temporal fluctuations is unknown. Odor responses in projection neurons, the targets of olfactory neurons, can be described by a linear-nonlinear model that represents odor fluctuations across the population, independent of odor identity (Geffen et al., 2009). This patterned projection neuron activity may encode temporal information about odors (Vickers et al., 2001; Brown et al., 2005), but it discards detailed information from individual peripheral neurons.

In *C. elegans*, our results suggest that ASH-specific and AWC-specific temporal information can be propagated through the nervous system without loss, since mutants with subtle changes in sensory neuron dynamics have matching changes in behavioral dynamics. This result was not obvious, as sensory neurons are not always temporally correlated with behaviors – vertebrate visual perception is much faster than cone photoreceptor integration times, which run to hundreds of milliseconds (Schnapf et al., 1990). Even where there is a correlation of sensory and perceptual timescales, as in the vertebrate auditory system (Eggermont et al., 1983), that general correlation does not automatically extend to the detailed temporal features of sensory neurons we describe here, and nor does it demonstrate the preservation of that temporal information across circuit levels.

Mapping ASH filter properties onto molecules and behaviors

ASH neurons initiate a nociceptive escape behavior with a latency of up to 10 s, depending on the strength of the repellent stimulus (Mellem et al., 2002; Chao et al., 2004). These behavioral dynamics match the ASH filter for high-osmolarity glycerol, which had a peak response at ∼3 s and a ∼10 s integration time. These values appear slow for an escape circuit, but the temporal filter does not determine how quickly a neuron can respond, and

indeed ASH depolarizes in response to aversive touch stimuli within a few milliseconds (Geffeney et al., 2011). Instead, the filter defines the time at which the neural response to a stimulus is strongest, and the interval over which the signal is integrated. Relatively slow filtering may allow ASH to evaluate noxious high osmolarity stimuli based on their strength, duration, and rate of change.

ASH temporal filters for high osmolarity glycerol and NaCl were similar, although they have different molecular receptors: the primary Na+ sensor, *tmc-1*, is not required for glycerol sensation (Chatzigeorgiou et al., 2013). However, ASH adapted quickly and did not support sustained responses to the repellents quinine and DHCA, suggesting heterogeneity in its temporal responses.

The ability to map mutations onto specific model features allowed a more detailed mapping of the LN-ODE models to molecular mechanisms and behavior. Based on previous studies, we expected the EGL-19 L-type voltage-activated calcium channel to amplify sensory signaling or generate a nonlinearity in the ASH glycerol response. Instead, an *egl-19* mutation preferentially affected the slow inverted component of the response, and its strongest effect on ASH calcium dynamics was on response decay. This observation predicted a reduction in behavioral adaptation to glycerol that was observed at similar timescales. Calcium initiates desensitization or adaptation in many sensory systems (Torre et al., 1995). Our results do indicate a small role of EGL-19 in the amplification of the signal, in agreement with other work (Hilliard et al., 2005), and there may be other cells and conditions in which EGL-19 is more important for the primary signal.

Rapid signaling in AWC supports active sensing

The apparent ability of AWC to detect odor gradients produced by sinusoidal head swings is an example of active sensing, in which an animal shapes the structure of sensory input through motor behavior (Schroeder et al., 2010), and perception requires sensory-motor integration (Saig et al., 2012). One requirement for active sensing is a sensory neuron that parses the environment within the time interval of the coupled motor behavior. Odor sensing in AWC neurons involves fast linear filters that peak in less than a second, a timescale matched to individual head swings. If the active sensing model is correct, rapid filtering of stimuli may be a general requirement for neurons that drive steering behavior in chemotaxis and thermotaxis. Notably, a temperature shift generates a current in thermosensitive AFD neurons that peaks at ∼500 ms (Ramot et al., 2008), a similar time frame as the rapid AWC response inferred here.

Among postsynaptic targets of AWC, the RIA neuron is a plausible target for detecting rapid AWC signals for steering, since it responds to AWC odors with calcium transients that are time-locked to sinusoidal head swings (Hendricks et al., 2011). By contrast, another target neuron, AIB, regulates turning and responds to AWC activation with a half-time of ten seconds (Chalasani et al., 2007). AIB might sense slower changes in AWC activity during the biased random walk behaviors that integrate odor responses over many seconds.

Rhythmic active sensing, such as sniffing, whisking and the head-swing related olfactory behavior studied here, performs best when sensory and motor systems operate not only at

matching frequencies, but in temporal phase with each other. The *odr-3* G-alpha protein mutation that slows the AWC filter suggests such a phase-matching feature, because it gave rise to altered steering behaviors, not the complete absence of steering. We speculate that a phase-dependent element of chemotaxis explains the stereotyped temporal response of AWC neurons across multiple odors and a 100-fold range of odor concentration. This invariance may maintain, across odors and odor concentrations, a tight match of sensory and motor dynamics for active sensation.

EXPERIMENTAL PROCEDURES

Calcium Imaging

Calcium imaging lines for ASH and AWC neurons expressed the genetically encoded calcium indicator GCaMP3 (Tian et al., 2009) under the *sra-6* and *str-2* promoters, respectively. One-day old adult worms were trapped in a custom-designed microfluidic device made of the transparent polymer polydimethylsiloxane (PDMS), where their noses were exposed to liquid streams under laminar flow (Chronis et al., 2007). Switching between odor streams was accomplished by controlling flow to two adjacent laminar side-streams, a protocol that minimized fluid pressure changes during odor delivery (Figure S1). Movement artifacts were minimized by adding a cholinergic agonist, 1 mM tetramisole, to the worm-loading channel. Tetramisole had no apparent effect on chemosensory responses in AWC or ASH neurons. Wide-field microscopy was used to simultaneously monitor GCaMP fluorescence from the cell of interest and fluorescein dye added to the stimulus channel. The measured dye fluorescence in each frame was used as a surrogate for odor concentration for modeling. Fluorescence signals were analyzed after a newly developed bleach-correction algorithm with gain correction (see Supplemental Experimental Procedures).

The m-sequence pulse length was limited to a minimum of 200 ms because of the mechanical limit of the microfluidic switch, assessed by tracking fluorescein. ASH calcium activity in response to 1 M glycerol (with fluorescein) had a near-fusion response to 200 ms flicker, indicating that the cell or sensor was close to its limit for tracking the stimulus; AWC responses were faster. Pseudo-random sequences were 2× repeats of 9-bit word length m-sequences, i.e. an m-sequence length of 2^9-1=511 pulses.

Dynamical Model Estimation and Correction for GCaMP3 Response Dynamics

We generated analytical versions of each filter with five free parameters by defining them to be the result of convolution of the putative GCaMP3 filter and the impulse response of a third-order linear system given by the following equations:

$$\frac{dA}{dt} = -k_a A + input$$

$$\frac{dF}{dt} = -k_f F + k_{af} A$$

$$\frac{dS}{dt} = -k_s S - k_{as} A$$

$$output = F + S$$

The linear filter arising from these equations is the impulse response, which is the solution for an input given by a δ-function and the initial condition *A(0)=B(0)=C(0)=0*, and is

$$K_{neuron}(t) = \frac{k_{af} e^{-k_f t}}{k_a - k_f} - \frac{k_{as} e^{-k_s t}}{k_a - k_s} + \frac{\left(k_{af}\left(k_s - k_a\right) - k_{as}\left(k_f - k_a\right)\right) e^{-k_a t}}{\left(k_a - k_f\right)\left(k_a - k_s\right)}$$

The optimal parameters of these filters were found by replacing linear regression with least squares Nelder-Mead optimization of the dynamical model parameters.

Recent fluorometry experiments have measured GCaMP responses to sharp (<1 ms mixing time) up and down steps of [Ca^{2+}] (Sun et al., 2013). In these experiments, the rate of change in fluorescence during a rise or fall in response to a calcium step is greatest immediately after the step transition and the fluorescence versus time curves do not show a discernable inflection point, suggesting that the GCaMP response is well described by a monotonically decaying filter. We modeled the filter as an decaying exponential $K_{GCaMP}=e^{-kt}$ where k= 1/(.4963) s^{-1}, corresponding to a $t_{½}$ decay time of .344 s (Sun et al., 2013). The convolution of the GCaMP filter and neuronal impulse can be computed in a straightforward manner to obtain an expression for the full filter. To analytically deconvolve the intrinsic neural impulse response, we fit the computed full filter expression to the observed data using linear regression as described in Extended Experimental Procedures. We then use the resulting optimized parameters in the expression for the neural filter $K_{neuron}(t)$.

Model Performance Evaluation

Performance of a model with respect to a particular input-output record was evaluated by computing the variance-accounted-for by the simulated output trace $\hat{y}$ versus the measured output trace y, according to

$$VAF = 100\% * \left(1 - \frac{var\left(y - \hat{y}\right)}{var\left(y\right)}\right)$$

A 100% VAF indicates that a model has perfect predictive power, whereas a 0% VAF indicates that a model has no more predictive power than a constant trace set equal to the mean response. The conversion from a “signal-to-residual” (SNR) value (Geffen et al., 2009) to a VAF value is given by the formula VAF=100%*(1-1/SNR^2).

Chemotaxis Assays

20∼30 adult animals were washed with S basal and assay buffer and placed on 10 cm square chemotaxis plates (1.6% agar, 1 mM MgSO4, 1 mM CaCl2, 5 mM phosphate buffer [pH 6.0]). 2 μl of 1:100 isoamyl alcohol was placed 2 cm from the origin, and a 20 minute video was recorded at 3 fps with Streampix software and a 6.6MP Pixelink PL-B781F camera, and tracked using MATLAB scripts to produce a set of tracks of the body centroid. For "pirouette" or turning frequency analysis, turns were identified and binned with respect to their incoming bearing angle in 15° intervals, following the method of Tsunozaki et al., 2008. For "weathervane" or steering analysis, track portions within 1 cm of the odor source on the animal's first approach to within 2 mm of the odor source were analyzed to detect curvature versus bearing, following the method of Iino and Yoshida, 2009. Portions of tracks with extremely high curving rates (>40 degrees/mm) were excluded from analysis. For recording of the movement trace in Figure 6G, assays were performed on 6 cm round chemotaxis plates recorded at ∼5 fps with a Macrofire Optronics camera and tracked using custom MATLAB scripts.

Glycerol Avoidance Assays

Young adult worms were removed from food, washed, and ∼25 animals injected into one arena of a custom-designed PDMS microfluidic device (Albrecht and Bargmann, 2011). Each arena contained a structured micropost array optimized for crawling locomotion, barriers to prevent animal escape, and inlet channels to deliver temporal pulses of glycerol. After 30 minutes of acclimation to the PDMS environment in continuously flowing S-basal buffer, animals were exposed to 30 s pulses of 500 mM glycerol alternating with 30 s pulses of buffer, controlled by automated valves (Lee Corporation) actuated by computer using a LabJack U3-hV digital controller, a Valvebank 8 II actuator (Automate), and custom MATLAB scripts. In each experiment, 30 pulses of glycerol were given in 34 minutes, with 2 minutes of buffer before and after the last stimulus pulse, and the entire sequence was repeated six times. Figure 5 shows results from the 2^{nd} to 8^{th} trials from all 30-trial series, in experiments gathered over 3-5 days for 12-20 arenas per genotype. Animals were recorded at 2 fps and analyzed using automated tracking software. Behaviors were segmented into forward locomotion, pauses, reversals, and omega turns, and animals in the forward locomotion state were also analyzed for speed, binned by 2 s intervals. A stimulus-aligned ethogram of instantaneous behavioral state was assembled for each trial and all 6 trials were averaged for each genotype.

Supplementary Material

Refer to Web version on PubMed Central for supplementary material.

Acknowledgments

S.K. developed analytical methods and models; Y.X. developed methods and analyzed ASH responses and behaviors; C.E.C. analyzed AWC responses and behaviors; S.K., L.F.A., and C.I.B. designed and interpreted experiments and wrote the manuscript. We thank L. Looger for GCaMP3.0 and B. Bamber, C. Niell, G. Wayne, M. Vidne, D. Rubin, and P. McGrath for their insights and their comments on the manuscript. This work was supported by the Gatsby, Swartz, and Kavli Foundations (L.F.A.), and the Howard Hughes Medical Institute (C.I.B.). S.K. was supported by NIH training grant T32NS064929 and NIMH grant R01MH93338, which also provided support

for L.F.A. C.E.C. was supported by the Department of Defense (DoD) through the National Defense Science & Engineering Graduate Fellowship (NDSEG) Program, and Y.X. was supported by MSTP grant GM07739 and a Paul and Daisy Soros Fellowship.

References

Albrecht DR, Bargmann CI. High-content behavioral analysis of *Caenorhabditis elegans* in precise spatiotemporal chemical environments. Nat. Methods. 2011; 8:599–605. [PubMed: 21666667]

Atick JJ, Redlich AN. Towards a theory of early visual processing. Neural Computation. 1990; 2:308–320.

Bargmann, CI. Chemosensation in *C. elegans* (October 25, 2006). *WormBook*, ed. The *C. elegans* Research Community, WormBook. 2006. doi/10.1895/wormbook.1.123.1, http://www.wormbook.org

Bhandawat V, Reisert J, Yau KW. Elementary response of olfactory receptor neurons to odorants. Science. 2005; 308:1931–1934. [PubMed: 15976304]

Brown SL, Joseph J, Stopfer M. Encoding a temporally structured stimulus with a temporally structured neural representation. Nat. Neurosci. 2005; 8:1568–1576. [PubMed: 16222230]

Busch KE, Laurent P, Soltesz Z, Murphy RJ, Faivre O, Hedwig B, Thomas M, Smith HL, de Bono M. Tonic signaling from O_2 sensors sets neural circuit activity and behavioral state. Nat. Neurosci. 2012; 15:581–591. [PubMed: 22388961]

Chalasani SH, Chronis N, Tsunozaki M, Gray JM, Ramot D, Goodman MB, Bargmann CI. Dissecting a circuit for olfactory behaviour in *Caenorhabditis elegans*. Nature. 2007; 450:63–70. [PubMed: 17972877]

Chao MY, Komatsu H, Fukuto HS, Dionne HM, Hart AC. Feeding status and serotonin rapidly and reversibly modulate a *Caenorhabditis elegans* chemosensory circuit. Proc. Natl. Acad. Sci. USA. 2004; 101:15512–15517. [PubMed: 15492222]

Chatzigeorgiou M, Bang S, Hwang SW, Schafer WR. *tmc-1* encodes a sodium-sensitive channel required for salt chemosensation in *C. elegans*. Nature. 2013; 494:95–99. [PubMed: 23364694]

Chronis N, Zimmer M, Bargmann CI. Microfluidics for in vivo imaging of neuronal and behavioral activity in *Caenorhabditis elegans*. Nat. Methods. 2007; 4:727–731. [PubMed: 17704783]

Clark DA, Bursztyn L, Horowitz MA, Schnitzer MJ, Clandinin TR. Defining the computational structure of the motion detector in *Drosophila*. Neuron. 2011; 70:1165–1177. [PubMed: 21689602]

Clark DA, Grant LC. The bacterial chemotactic response reflects a compromise between transient and steady-state behavior. Proc. Natl. Acad. Sci. USA. 2005; 102:9150–9155. [PubMed: 15967993]

DasGupta S, Waddell S. Learned odor discrimination in *Drosophila* without combinatorial odor maps in the antennal lobe. Curr. Biol. 2008; 18:1668–1674. [PubMed: 18951022]

Dayan, P.; Abbott, LF. MIT Press; Cambridge MA: 2001. Theoretical Neuroscience: Computational and Mathematical Modeling of Neural Systems.

DeAngelis GC, Ohzawa I, Freeman RD. Receptive-field dynamics in the central visual pathways. Trends Neurosci. 1995; 18:451–458. [PubMed: 8545912]

Eggermont JJ, Johannesma PIM, Aertsen AMHJ. Reverse correlation methods in auditory research. Quart. Rev. Biophys. 1983; 16:341–414.

Fairhall AL, Lewen GD, Bialek W, de Ruyter Van Steveninck RR. Efficiency and ambiguity in an adaptive neural code. Nature. 2001; 412:787–702. [PubMed: 11518957]

Geffen MN, Broome BM, Laurent G, Meister M. Neural encoding of rapidly fluctuating odors. Neuron. 2009; 61:570–586. [PubMed: 19249277]

Geffeney SL, Cueva JG, Glauser DA, Doll JC, Lee TH-C, Montoya M, Karania S, Garakani AM, Pruitt BL, Goodman MB. DEG/ENaC but not TRP channels are the major mechanoelectrical transduction channels in a *C. elegans* nociceptor. Neuron. 2011; 71:845–857. [PubMed: 21903078]

Getahun MN, Wicher D, Hansson BS, Olsson SB. Temporal response dynamics of *Drosophila* olfactory sensory neurons depends on receptor type and response polarity. Front. Cell. Neurosci. 2012; 6:54. [PubMed: 23162431]

Goodman MB, Hall DH, Avery L, Lockery SR. Active currents regulate sensitivity and dynamic range in *C. elegans* neurons. Neuron. 1998; 20:763–772. [PubMed: 9581767]

Hendricks M, Ha H, Maffey N, Zhang Y. Compartmentalized calcium dynamics in a *C. elegans* interneuron encode head movement. Nature. 2012; 487:99–103. [PubMed: 22722842]

Hilliard MA, Apicella AJ, Kerr R, Suzuki H, Bazzicalupo P, Schafer WR. In vivo imaging of *C. elegans* ASH neurons: cellular response and adaptation to chemical repellents. EMBO J. 2005; 24:63–72. [PubMed: 15577941]

Iino Y, Yoshida K. Parallel use of two behavioral mechanisms for chemotaxis in *Caenorhabditis elegans*. J. Neurosci. 2009; 29:5370–5380. [PubMed: 19403805]

Izquierdo EJ, Lockery SR. Evolution and analysis of minimal neural circuits for klinotaxis in *Caenorhabditis elegans*. J. Neurosci. 2010; 30:12908–12917. [PubMed: 20881110]

Jones LM, Depireux DA, Simons DJ, Keller A. Robust temporal coding in the trigeminal system. Science. 2004; 304:1986–1989. [PubMed: 15218153]

Kim AJ, Lazar AA, Slutskiy YB. System identification of *Drosophila* olfactory sensory neurons. J. Comp. Neurosci. 2011; 30:143–161.

Koehl MAR, Reidenbach MA. The spatial and temporal patterns of odors sampled by lobsters and crabs in a turbulent plume. J. Exp. Biol. 2011; 214:3138–3153. [PubMed: 21865526]

Liu Q, Hollopeter G, Jorgensen EM. Graded synaptic transmission at the *Caenorhabditis elegans* neuromuscular junction. Proc. Natl. Acad. Sci. USA. 2009; 106:10823–10828. [PubMed: 19528650]

Marmarelis VZ, McCann GD. A family of quasi-white random signals and its optimal use in biological system identification. Part II: application to the photoreceptor *Calliphora erythrocephala*. Biol. Cyber. 1977; 27:57–62.

Martelli C, Carlson JR, Emonet T. Intensity invariant dynamics and odor-specific latencies in olfactory receptor neuron response. J. Neurophysiol. 2013; 33:6285–6297.

Massot C, Schneider AD, Chacron MJ, Cullen KE. The vestibular system implements a linear–nonlinear transformation in order to encode self-motion. PLoS Biol. 2012; 10:e1001365. [PubMed: 22911113]

Mellem JE, Brockie PJ, Zheng Y, Madsen DM, Maricq AV. Decoding of polymodal sensory stimuli by postsynaptic glutamate receptors in C. *elegans*. Neuron. 2002; 36:933–944. [PubMed: 12467596]

Nagel KI, Doupe AJ. Organizing principles of spectro-temporal encoding in the avian primary auditory area field L. Neuron. 2008; 58:938–955. [PubMed: 18579083]

Nagel KI, Wilson RI. Biophysical mechanisms underlying olfactory receptor neuron dynamics. Nat. Neurosci. 2011; 14:208–216. [PubMed: 21217763]

Pierce-Shimomura JT, Morse TM, Lockery SR. The fundamental role of pirouettes in *Caenorhabditis elegans* chemotaxis. J. Neurosci. 1999; 19:9557–9569. [PubMed: 10531458]

Ramot D, MacInnis BL, Goodman MB. Bidirectional temperature-sensing by a single thermosensory neuron in *C. elegans*. Nat. Neurosci. 2008; 11:908–915. [PubMed: 18660808]

Riffell JA, Abrell L, Hildebrand JG. Physical processes and real-time chemical measurement of the insect olfactory environment. J. Chem. Ecology. 2008; 34:837–853.

Roayaie K, Crump JG, Sagasti A, Bargmann CI. The G alpha protein ODR-3 mediates olfactory and nociceptive function and controls cilium morphogenesis in *C. elegans* olfactory neurons. Neuron. 1998; 20:55–67. [PubMed: 9459442]

Saig A, Gordon G, Assa E, Arieli A, Ahissar E. Motor-sensory confluence in tactile perception. J. Neurosci. 2012; 32:14022–14032. [PubMed: 23035109]

Sakai HM, Naka K-I, Korenberg MJ. White-noise analysis in visual neuroscience. Vis. Neurosci. 1988; 1:287–296. [PubMed: 3154801]

Segall JE, Block SM, Berg HC. Temporal comparisons in bacterial chemotaxis. Proc. Natl. Acad. Sci. USA. 1986; 83:8987–8991. [PubMed: 3024160]

Schnapf JL, Nunn BJ, Meister M, Baylor DA. Visual transduction in cones of the monkey *Macaca fascicularis*. J. Physiol. 1990; 427:681–713. [PubMed: 2100987]

Schroeder CE, Wilson DA, Radman T, Scharfman H, Lakatos P. Dynamics of active sensing and perceptual selection. Curr. Op. Neuro. 2010; 20:172–176.

Shusterman R, Smear M, Koulakov A, Rinberg D. Precise olfactory responses tile the sniff cycle. Nat. Neurosci. 2011; 14:1039–1044. [PubMed: 21765422]

Sun XR, Badura A, Pacheco DA, Lynch LA, Schneider ER, Taylor MP, Hogue IB, Enquist LW, Murthy M, Wang SS-H. Fast GCaMPs for improved tracking of neuronal activity. Nat. Commun. 2013; 4:2170. [PubMed: 23863808]

Suzuki H, Thiele TR, Faumont S, Ezcurra M, Lockery SR, Schafer WR. Functional asymmetry in *Caenorhabditis elegans* taste neurons and its computational role in chemotaxis. Nature. 2008; 454:114–117. [PubMed: 18596810]

Tian L, Hires SA, Mao T, Huber D, Chiappe ME, Chalasani SH, Petreanu L, Akerboom J, McKinney SA, Schreiter ER, et al. Imaging neural activity in worms, flies and mice with improved GCaMP calcium indicators. Nat. Methods. 2009; 6:875–871. [PubMed: 19898485]

Torre V, Ashmore JF, Lamb TD, Menini A. Transduction and adaptation in sensory receptor cells. J. Neurosci. 1995; 15:7757–7768. [PubMed: 8613717]

Tsunozaki M, Chalasani S, Bargmann CI. A behavioral switch: cGMP and PKC signaling in olfactory neurons reverses odor preference in *C. elegans*. Neuron. 2008; 59:959–971. [PubMed: 18817734]

Vickers NJ, Christensen TA, Baker TC, Hildebrand JG. Odour-plume dynamics influence the brain's olfactory code. Nature. 2001; 410:466–470. [PubMed: 11260713]

Wes PD, Bargmann CI. *C. elegans* odour discrimination requires asymmetric diversity in olfactory neurons. Nature. 2001; 410:698–701. [PubMed: 11287957]

Westwick, DT.; Kearney, RE. Wiley & Sons, Inc.; Hoboken, NJ: 2003. Identification of nonlinear physiological systems.

Zimmer M, Gray JM, Pokala N, Chang AJ, Karow DS, Marletta MA, Hudson ML, Morton DB, Chronis N, Bargmann CI. Neurons detect increases and decreases in oxygen levels using distinct guanylate cyclases. Neuron. 2009; 61:865–879. [PubMed: 19323996]

Highlights

- *C. elegans* AWC and ASH sensory neurons respond reliably to rapidly flickering stimuli
- Linear-nonlinear models of AWC and ASH reveal biphasic, near-linear temporal filters
- AWC filters are rapid (< 1 s) and invariant across odors; ASH filters are slower
- Slowing the AWC filter disrupts a fast steering behavior that requires active sensing

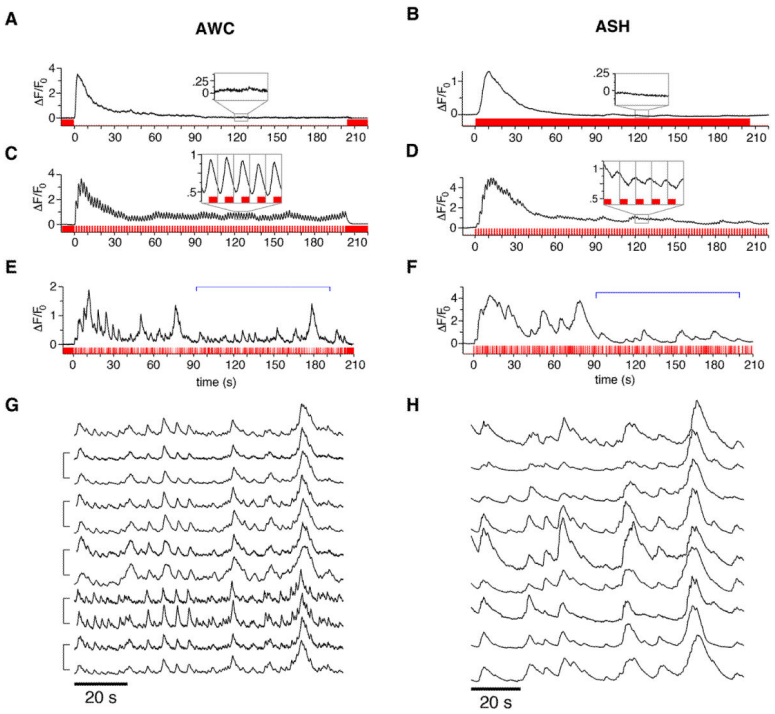

Figure 1. AWC and ASH Respond Reliably to Simple and Complex Odor Patterns

Representative calcium transients (black) of AWC or ASH neurons expressing GCaMP3; stimulus input sequences are shown in red. For methods see Figure S1.

(A,B) Step responses. (A) AWC response to odor removal after a five minute pre-exposure to 9.2×10^{-4} M isoamyl alcohol. (B) ASH response to addition of 1 M glycerol.

(C,D) Flicker responses. (C) AWC response to a flickering on/off 9.2×10^{-4} M isoamyl alcohol stimulus with a 1 s pulse length, following five minute pre-exposure to isoamyl alcohol. (D) ASH response to a flickering on/off 1 M glycerol stimulus with a 1 s pulse length. Insets, magnified views of 10 s intervals after the response reached steady-state, stimulus in red. Gray vertical lines divide the inset graphs into 2 s epochs aligned to stimulus transitions.

(E-H) Responses to pseudo-random m-sequence stimuli. (E) AWC response to a pseudo-random on/off 9.2×10^{-4} M isoamyl alcohol stimulus following a five-minute pre-exposure to isoamyl alcohol. (F) ASH response to a pseudo-random off/on pattern of 1 M glycerol. (E) and (F) used two repetitions of an m-sequence of pulse length 200 ms, 9-bit sequence. Brackets mark the second repetition, shown for additional neurons in (G) and (H), and used to construct and analyze the L-N model. The m-sequence stimulus input patterns were similar but with inverted sign; note the similar overall shape of the AWC and ASH neuronal responses but sharper temporal resolution in AWC traces. (G,H) Responses of additional AWC (G) or ASH (H) neurons to the same m-sequence as in (E) and (F). Brackets indicate two trials of a single animal, separated by ∼10 minutes. Individual traces were normalized to the peak magnitude within each trace.

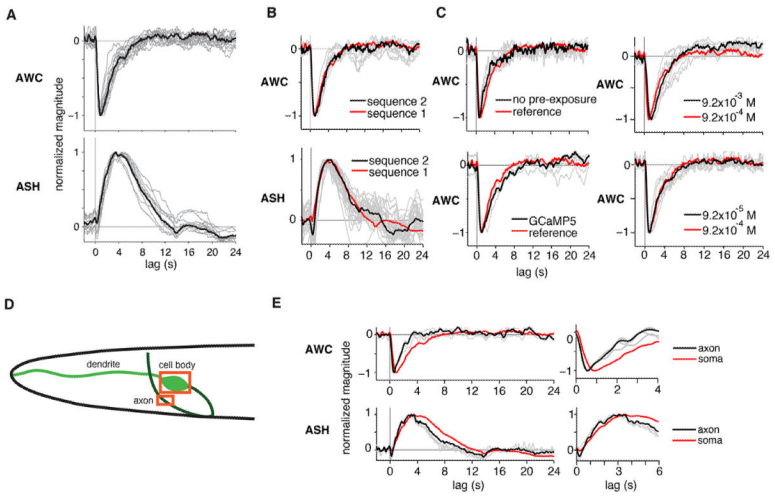

Figure 2. AWC and ASH Linear Filters are Invariant and Robust

(A) Linear filters inferred from individual input-output records for AWC and ASH neurons (gray) and from trial-averaged input-output records (black).

(B) AWC and ASH linear filters inferred from different m-sequence stimuli (sequence 2) compared to reference sequence from (A). Note the slight difference in ASH filters at late time points; an average of the two filters would likely reduce finite-length trial effects and provide a more accurate estimate of the “true” neural filter.

(C) AWC linear filters derived without odor pre-exposure, using a GCaMP5 indicator, and in response to different isoamyl alcohol concentrations. For concentration analysis of ASH filters, see Figure S3.

(D) Diagram of ASE or AWC anatomy, showing example regions of interest (boxes) for calcium imaging from the soma and axon.

(E) Comparison of linear filters from somatic (red) versus axonal (black) calcium signals in AWC and ASH, with early timepoints magnified at right.

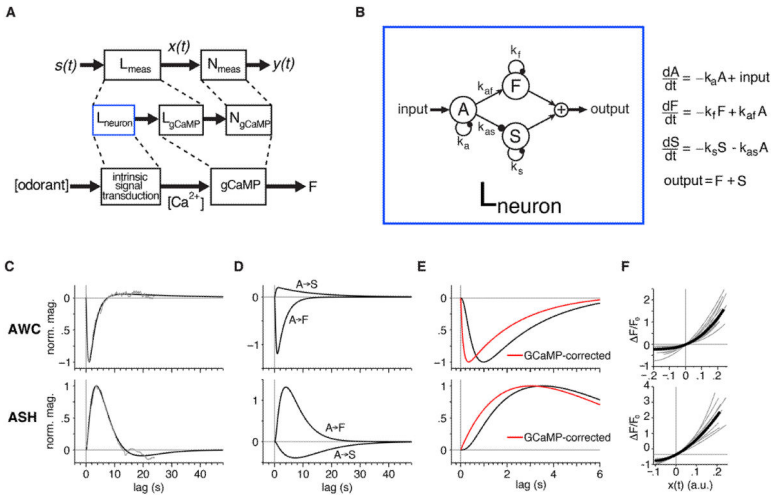

Figure 3. A Three-Variable ODE Model Produces a Biphasic Filter with Two Timescales

(A) Schematic of the overall linear-nonlinear model and putative mapping to elements of the signaling-to-GCaMP transformation. $L_{measured}$ (L_{meas}) is a convolution of the intrinsic neuronal filter L_{neuron} and the GCaMP filter L_{gCaMP}. The nonlinearity $N_{measured}$ (N_{meas}) probably arises predominantly from the GCaMP nonlinearity N_{gCaMP}.

(B) Diagram and equations of a three-variable ODE model that produces a biphasic filter with distinct timescales for each phase, corresponding to the L_{neuron} filter in (A). See also Table S1.

(C) Overall ODE model filter (in black) fit to the filter extracted from trial-averaged input-output records (in gray) for AWC and ASH. Technical issues limited the maximum lag of the estimated filters to 24 s, but the ODE model filters are extrapolated to 48 s.

(D) Decomposition of ODE model filter into fast (A-F) and slow (A-S) components corresponding to transformations between the input and outputs of variable F and S in (B). The sum of these component filters produces the full ODE filter in (C).

(E) In black, the first six seconds of overall model filters for AWC and ASH. In red, the intrinsic neuronal filter L_{neuron} analytically deconvolved from the overall filter L_{meas} to remove the dynamical effect of GCaMP3 (Tian et al., 2009; Sun et al., 2013).

(F) Normalized power-law nonlinearities for AWC and ASH obtained from individual input-output records (gray) and from trial-averaged input-output records (black). See also Figure S2.

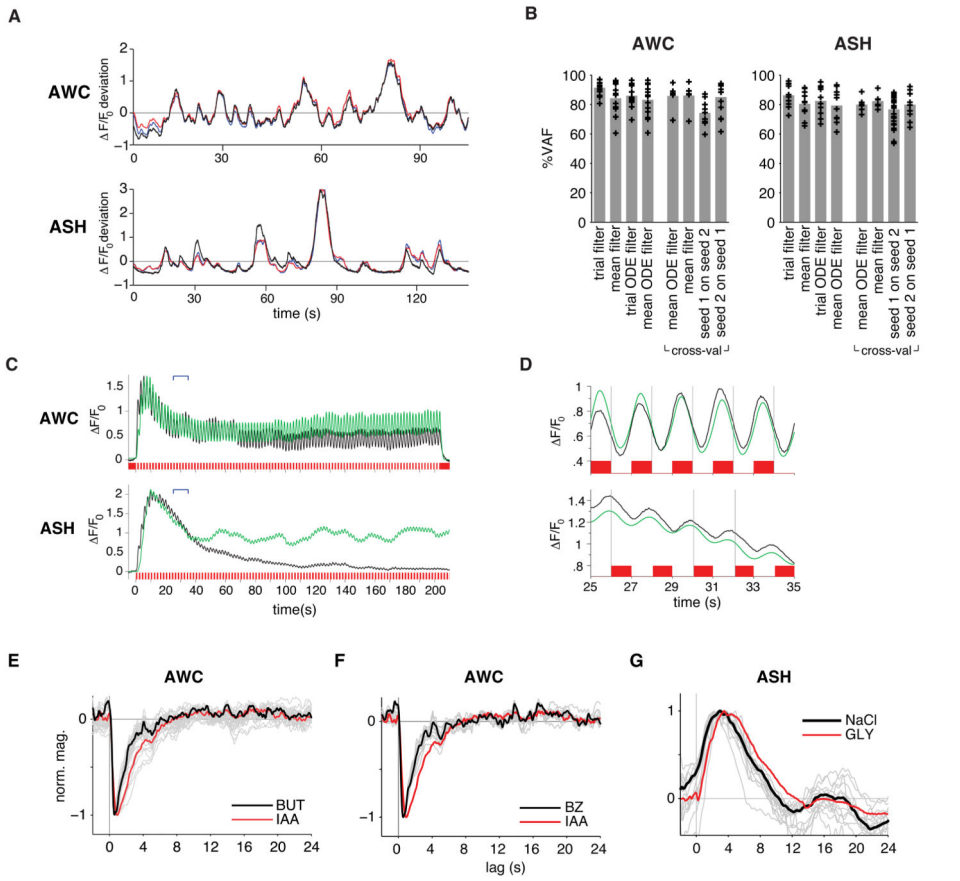

Figure 4. Linear-Nonlinear Models Capture the Dynamics of AWC and ASH Responses

(A) Actual (black) and simulated (red, blue) responses of representative AWC and ASH neurons to fluctuating stimuli. Simulations used a full-parameter L-N model with filters estimated from trial averaged input-output records (blue) or the ODE filter model (red).

(B) Performance (%VAF, per cent variance accounted for) of simulated individual trial responses using: (1) full-parameter L-N models estimated from individual trials (2) L-N model estimated from mean trial-averaged records, (3) ODE filter L-N model estimated from individual trials, and (4) ODE filter L-N model estimated from mean trial-averaged records. Cross-val, cross-validated performance of simulating individual trial responses from held-out datasets using: (5) ODE filter L-N model estimated from mean trial-averaged records, (6) trial-averaged L-N model applied to a cross validation set, (7) mean trial-averaged L-N model applied to a hold-out set driven by a second m-sequence stimulus, and (8) mean trial-averaged L-N model estimated from the second m-sequence set tested on trials of the first m-sequence. Bars indicate average performance. n=14 for AWC, n=10 for ASH, and n=7 for both cross-validation sets.

(C) In green, simulated responses to trial-averaged 1 s ON/OFF square pulse input records using the mean ODE filter L-N model for AWC and ASH. Actual trial-averaged output records are in black (n=12 for each neuron). Brackets indicate time period excerpted in (D). The ODE models do not describe response magnitude; they were scaled to the peak response.

(D) Magnified excerpt of predicted (green) and actual (black) responses in (C) from t=25-35 seconds. Gray vertical lines divide the inset graphs into 2 s epochs aligned to stimulus transitions.

(E and F) AWC filters to butanone (1.11×10^{-5} M, n=27), and (F) benzaldehyde (9.8×10^{-4} M, n=10). Trial-averaged filters are in black and individual trial filters in grey; red is isoamyl alcohol reference.

(G) ASH filter for NaCl (500 mM, n=13). Trial-averaged filter is in black and individual trial filters in grey; red is 1 M glycerol reference.

See also Figures S4, S5, and S6.

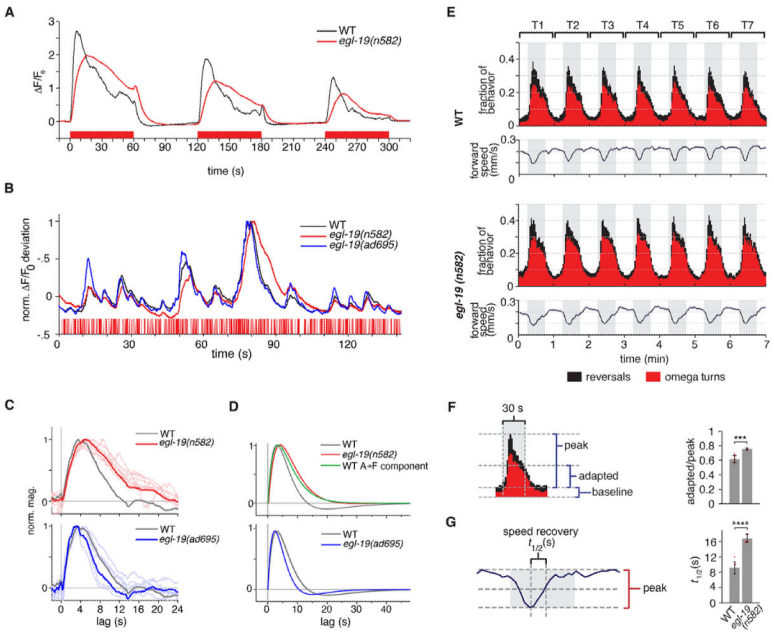

Figure 5. An *egl-19* Calcium Channel Mutant Shows Matching Defects in ASH Calcium Dynamics and Behavioral Adaptation.

(A) Average responses of ASH wild type (n=7) and *egl-19(n582)* (n=23) mutants to 60 s on/off pulses of 1 M Gly, stimulus shown below in red. See also Figures S3 and S5.

(B) Excerpt of trial-averaged responses to 200 ms glycerol m-sequences of ASH wild type (n=10), *egl-19(n582)* reduction-of-function mutants (n=7), and *egl-19(ad695gf)* gain-of-function mutants (n=7), stimulus shown below in red.

(C) Linear filter measured from ASH neurons of *egl-19(n582)* mutant (upper panel) and *egl-19(ad695gf)* mutant (lower panel) trial-averaged records (thick lines) and individual records (thin lines) compared to wild-type filter (gray).

(D) ODE model filter for ASH from *egl-19(n582)* mutant (upper panel) and *egl-19(ad695gf)* mutant (lower panel) trial-averaged records (red, blue) compared to the wild type ODE filter (gray). The *egl-19(n582)* ODE filter closely matches the ASH wild type fast pathway (A-F) filter from Figure 3D, shown here in green. See also Table S1.

(E) Behavioral analysis of *egl-19(n582)* avoidance responses to 500 mM glycerol. Reversals (black) and omega turns (red) (upper traces) and speed changes (dark blue line, lower traces) are avoidance behaviors elicited upon encountering the high-osmolarity stimulus. Results are shown for seven successive 30 s pulses of glycerol (gray) alternating with 30 s of S Basal buffer (white), with behaviors binned every 2 s.

(F,G) The seven pulses from (E) were averaged into a single stimulus-aligned response to 500 mM glycerol (illustrated for WT in left panels) and analyzed in right panels (1420 tracks for WT, 868 tracks for *egl-19(n582)*). (F) Fraction of animals exhibiting reversal and omega behavior in the last bin of a 30 s pulse period (“adapted”) divided by the maximum fraction exhibiting reversals or omegas in any bin (“peak”) for each of seven consecutive pulses. Error bars indicate s.d., *** P=0.0002, Welch’s two-tailed t-test.

(G) Average time to half-recovery of baseline forward speed after glycerol encounter. Error bars indicate s.d., **** P<0.0001, Welch’s two tailed t-test.

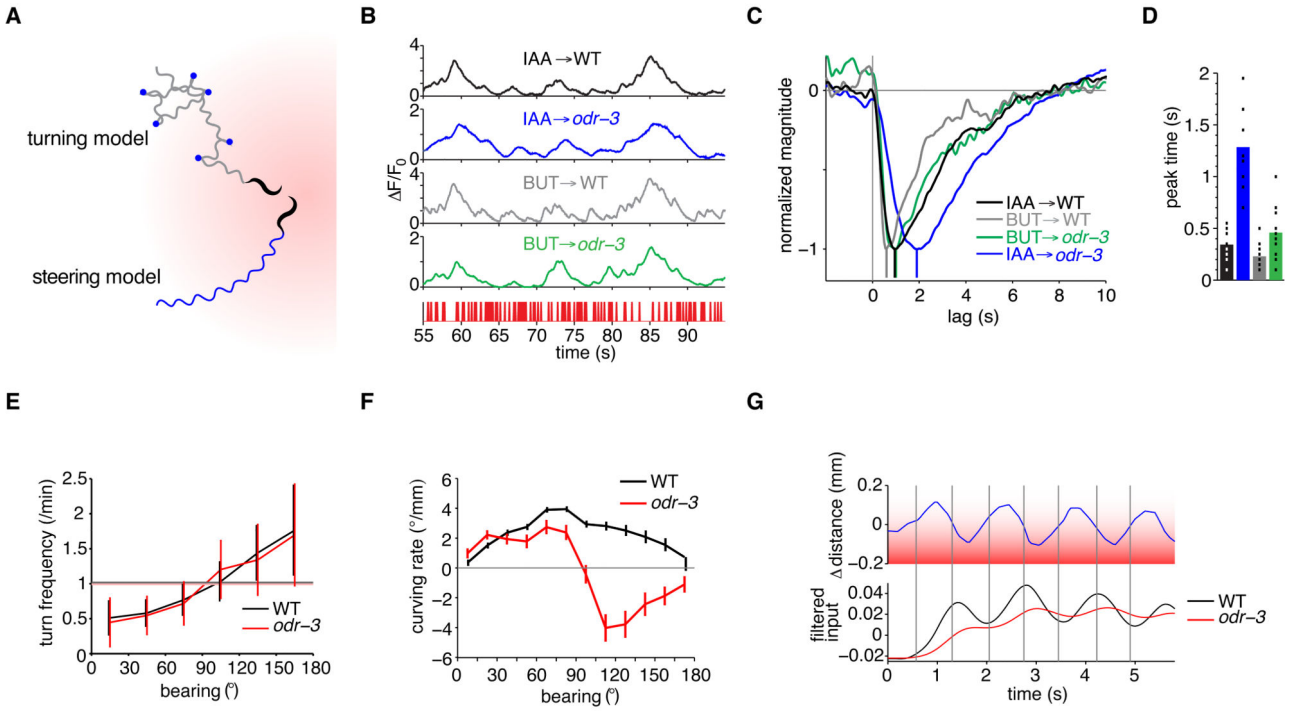

Figure 6. The ODR-3 G-alpha Protein Affects The Rapid AWC Filter and Steering During Chemotaxis

(A) Schematic of two distinct chemotaxis strategies in an odor gradient, shown shaded red. A biased random walk turning strategy (top path) consists of bouts of forward runs punctuated by sharp, randomly directed turns (blue dots) whose frequency is modulated by the rate of concentration change. The steering strategy (bottom path) uses gradual, directed corrections to the path direction during forward runs to orient the head toward the gradient.

(B) Segment of wild-type and *odr-3(n2150)* responses to an m-sequence of 9.2×10^{-4} M isoamyl alcohol (IAA) and 1.11×10^{-5} M butanone (BUT). The stimulus sequence is shown at bottom in red. Note the coarser temporal resolution of the *odr-3* IAA response, suggesting that this neuron does not follow stimuli as quickly.

(C) Trial-averaged AWC linear filters for wild type and *odr-3* responses to IAA and BUT, normalized to peak. Colors match traces in (B).

(D) Peak times of individual trial filters, corrected for GCaMP3 kinetics, for wild type and *odr-3* responses to IAA and BUT. Colors match traces in (C). For C-D, n=11-27 traces per condition. In (D), WT IAA differs from BUT ($P<0.001$), WT IAA differs from *odr-3* IAA ($P<0.001$), and WT BT differs from *odr-3* BUT ($P=0.0013$) by Welch's two-tailed t-test. See also Figure S6.

(E) Both WT and *odr-3* suppress turning when moving toward the odor (0° bearing) and increase turning when moving away from the odor (180° bearing), with a positively increasing relationship, the signature of a biased random walk. Turning events were counted across 60 tracks for each strain during a 20 minute assay. Error bars indicate s.e.m.

(F) Curving rate versus bearing reveals a defect in steering in *odr-3* relative to WT at bearings ≥ 90 degrees. When moving away from the odor source, *odr-3* animals curve in the

wrong direction. Data are taken from three assays per genotype, with 10-20 animals per assay. Error bars indicate s.e.m.

(G) Tracked distance from the head of a worm to an odor source, relative to the mean head-to-source distance along the track segment, versus time. This representative track was made during a forward run at a bearing of 90 degrees to an odor source ∼1 cm away (in red). Bottom plot: “perception signals” simulated by convolving the head position with the empirical trial-average isoamyl alcohol ODE filters for AWC in WT (black) and *odr-3* (red). The *odr-3* perception signal is attenuated and phase lagged relative to WT.